

# Constraints on Bosonic Dark Matter with Low Threshold Germanium Detector at Kuo-Sheng Reactor Neutrino Laboratory

Manoj Kumar Singh<sup>a,b</sup>, Lakhwinder Singh<sup>a,\*</sup>, Mehmet Agartioglu<sup>a,c</sup>,  
Vivek Sharma<sup>a,b,\*</sup>, Venktesh Singh<sup>b</sup>, Henry Tsz-king Wong<sup>a</sup>

<sup>a</sup>*Institute of Physics, Academia Sinica, Taipei 11529, Taiwan*

<sup>b</sup>*Department of Physics, Institute of Science, Banaras Hindu University, Varanasi 221005, India*

<sup>c</sup>*Department of Physics, National Dong Hwa University, Shoufeng, Hualien 97401, Taiwan*

---

## Abstract

We report results from searches of pseudoscalar and vector bosonic super-weakly interacting massive particles (super-WIMP) in the TEXONO experiment at the Kuo-Sheng Nuclear Power Station, using 314.15 kg days of data from  $n$ -type Point-Contact Germanium detector. The super-WIMPs are absorbed and deposit total energy in the detector, such that the experimental signatures are spectral peaks corresponding to the super-WIMP mass. Measured data are compatible with the background model, and no significant excess of super-WIMP signals are observed. We derived new upper limits on couplings of electrons with the pseudoscalar and vector bosonic super-WIMPs in the sub-keV mass region, assuming they are the dominant contributions to the dark matter density of our galaxy.

*Keywords:* Germanium Detectors, Data Acquisition, Bosonic Dark Matter, super-WIMP

---

\*Corresponding author

*Email addresses:* lakhwinder@gate.sinica.edu.tw (Lakhwinder Singh),  
vsharma@gate.sinica.edu.tw (Vivek Sharma)

## 1. Introduction

There is ample evidence for the existence of dark matter (DM) that come from numerous astronomical and cosmological observations at different scales. Since all the existing evidence only probe the gravitational interaction of DM, their non-gravitational interactions with normal matter are still elusive. Many extensions of the standard model (SM) of particle physics predict viable DM candidates. Weakly Interacting Massive Particles (WIMP), axions or axion-like particles (ALPs), sterile neutrinos and millicharged particles are leading candidates of DM. Searches for these leading candidates are in full swing, but an experimental verification via direct, indirect detection or production from LHC is still awaited. In the absence of a credible positive signal, direct detection experiments have ruled out a substantial portion of the favored WIMP parameter space in the GeV to TeV mass range [1, 2]. The light-DM (LDM) has received more attention at both theoretical and experimental front in recent years. Bosonic super-weakly interacting particles (denoted by  $\chi$ ) constitute another large category of LDM candidates with masses at the keV-scale [3]. These bosonic  $\chi$  candidates are experimentally very interesting due to their absorption via ionization or excitation of an electron in the target-atom of detectors. The bosonic  $\chi$  would deposit the energy equivalent to their rest mass in the detector. A photo-like peak with unexplained origin in the measured energy spectrum would be “smoking gun” signature of bosonic LDM. Point-Contact Germanium (PCGe) detectors [4] with their excellent energy resolution, sub-keV threshold, and low intrinsic radioactivity background are the best candidates to study LDM and other physics beyond the SM.

The theme of this article is to report improved direct laboratory limits on  $\chi$  coupling based on the data acquired by an n-type Point-Contact Germanium (*n*PCGe) detector at the Kuo-Sheng Reactor Neutrino Laboratory (KSNL). The structure of this report is as follows. Section 2 describes the interaction and expected rate of  $\chi$  at Ge target. Highlights of the experimental setup and data acquisition at KSNL are presented in Sec. 3. The performance parameters

of the  $n$ PCGe detector are summarized in Sec. 4. The detail of event selection of candidates and background suppression is explained in Sec 5. We present our results compared with the other representative experiments in Sec. 6. Finally, we conclude in Sec. 7.

## 2. Bosonic Dark Matter

Pseudoscalar, scalar, and vector are three generic possible candidates of non-relativistic LDM that may have a superweak coupling with SM particles. The correct relic density of bosonic LDM in a wider mass range could be obtained via either thermally or non-thermally misalignment mechanism [5, 6, 7]. The bosonic pseudoscalar ( $\chi_{\text{ps}}$ ) are excellent candidates of LDM. The effective interaction Lagrangian of pseudoscalar-LDM particles with the electron is given as

$$\mathcal{L}_{int} = \frac{g_{aee}}{2m_e} (\partial_\mu a) \bar{\psi} \gamma^\mu \gamma^5 \psi, \quad (1)$$

where  $a$  is the bosonic pseudoscalar field,  $g_{aee}$  is the pseudoscalar-electron coupling constant,  $m_e$  is the mass of electron,  $\gamma^\mu$  are the Dirac matrices, and  $\bar{\psi}$ ,  $\psi$  are dual Dirac spinors. The phenomenology behind  $\chi_{\text{ps}}$  is similar to nonrelativistic ALPs. The  $\chi_{\text{ps}}$  have coupling to atoms through the axioelectric effect:

$$\chi + A \rightarrow A^+ + e^-, \quad (2)$$

which is analogous to the photoelectric effect with the absorption of  $\chi_{\text{ps}}$  instead of a photon [8]. The only difference between photoelectric effect and axioelectric effect is the wave function of absorbed photon and  $\chi_{\text{ps}}$ . The wave function of absorbed photon contains a space-dependent factor  $\exp(i\mathbf{k}\mathbf{r})$ , which is replaced by  $\exp(im_{\text{ps}}\mathbf{v}_\chi\mathbf{r})$  in case of massive  $\chi_{\text{ps}}$  [3]. Here  $m_{\text{ps}}$  and  $v_\chi$  are the mass and velocity of the incoming  $\chi_{\text{ps}}$  particle, respectively. The absorption cross section  $\sigma_{abs}$  (axio-electric effect) for  $\chi_{\text{ps}}$  can be written as

$$\sigma_{abs} \simeq \frac{3m_{\text{ps}}^2}{4\pi\alpha f_a^2 \beta} \sigma_{pe}(w = m_{\text{ps}}), \quad (3)$$

where  $\sigma_{pe}$  is the photoelectric cross section with the photon energy  $\omega$  replaced by the mass of  $\chi_{ps}$  ( $m_{ps}$ ),  $f_a = 2m_e/g_{aee}$  is the dimensionless coupling strength of  $\chi_{ps}$  to SM particles and  $\beta \equiv v_\chi/c$ . The absorption cross section of  $\chi_{ps}$  is directly proportional to  $m_{ps}^2$ .

The best motivated model for bosonic vector dark matter ( $\chi_v$ ) is kinetic mixing model, in which an extra  $U(1)_D$  gauge group is introduced into SM gauge group. The kinetic mixing with the hypercharge field strength is responsible for the interaction between the ordinary matter and  $\chi_v$ . The interaction Lagrangian density for  $\chi_v$  with electrons after breaking of  $U(1)_D$  can be expressed as

$$\mathcal{L}_{int} = \kappa e V_\mu \bar{\psi} \gamma^\mu \psi, \quad (4)$$

where  $V_\mu$  is the bosonic vector field couples to the electromagnetic current,  $e$  is the electronic charge,  $\kappa$  is the vector hypercharge. The product  $e' = e\kappa$  is analogous to electromagnetic coupling such that  $\alpha' = (e\kappa)^2/4\pi$  is similar to a vector-electric fine-structure constant. The Compton wavelength of  $\chi_v$  is much larger than the linear dimension of the atom due to nonrelativistic behavior. This allow the multipole expansion in the interaction. The contribution of E1-transition dominates over other multipoles [9], which makes the matrix element of photon absorption proportional to the matrix element of  $\chi_v$  absorption. The absorption cross section of  $\chi_v$  ( $\sigma_{abs}$ ) can be expressed in the photoelectric effect with the replacement of photon energy  $\omega$  by the mass  $m_v$  of  $\chi_v$  and the coupling constant is scaled appropriately as [3]

$$\frac{\sigma_{abs}}{\sigma_{pe}(\omega = m_v)} \simeq \frac{\alpha'}{\alpha} \frac{1}{\beta}. \quad (5)$$

The absorption cross section of  $\chi_v$  is nearly independent of the DM mass.

The key difference between  $\chi_{ps}$  and  $\chi_v$  LDM is their decay modes to photons. The two-photon decay channel is strictly forbidden for vector boson, whereas decay into three photons is allowed at loop level [9]. Pseudoscalar bosons are axion-like with two-photon decay as a dominant channel. The mass of a scalar particle receives quadratically radiative contributions from its interactions with

other SM particles. The keV-scale bosonic scalar ( $\chi_s$ ) requires highly model dependent parameters in order to make it viable candidates. The phenomenology of  $\chi_s$  is also quite similar to the  $\chi_{ps}$  in many ways [3]. Experimental searches thus mainly focus on  $\chi_{ps}$  and  $\chi_v$ .

Assuming the  $\chi$  ( $\chi_{ps}$  or  $\chi_v$ ) constitutes all of the galactic DM with their local density  $\rho_\chi = 0.3 \text{ GeV}/\text{cm}^3$ , the total average flux of  $\chi$  ( $\Phi_\chi = \rho_\chi v_\chi / m_\chi$ ) is given by

$$\Phi_\chi = \frac{9.0 \times 10^{15}}{m_\chi} \times \beta \text{ cm}^{-2}\text{s}^{-1}, \quad (6)$$

where  $m_\chi$  is the mass of  $\chi$  in  $\text{keV}/c^2$ ,  $v_\chi$  is the average velocity of  $\chi$  relative to the Earth;  $\beta \equiv v_\chi/c \sim 10^{-3}$  implies that the energy deposition by bosonic  $\chi$  would be  $E = \sqrt{(m_\chi^2 + \gamma^2 m_\chi^2 \beta^2)} \sim m_\chi$ .

The theoretically expected interaction rate of  $\chi$  in a direct detection experiment can be expressed as

$$R_\chi = \rho_d \sigma_{abs} \Phi_\chi, \quad (7)$$

where  $\rho_d = N_A/A$  is the atomic number density per unit target mass of detector and  $N_A$  is the Avogadro's number.  $\sigma_{abs}$  is the absorption cross section of  $\chi$ . The interaction rate of  $\chi_{ps}$  in the units of  $\text{kg}^{-1}\text{day}^{-1}$  can be calculated by using the Eq. 7. Accordingly, the expected rate becomes

$$R_{ps} \simeq \frac{1.2 \times 10^{19}}{A} g_{aee}^2 \frac{m_{ps}}{[\text{keV}]} \frac{\sigma_{pe}}{[\text{barns}]} \text{kg}^{-1}\text{day}^{-1}, \quad (8)$$

where  $A$  is the atomic mass of target materials. Similarly, the expected count rate of  $\chi_v$  in the direct detection experiment can be expressed as

$$R_v \simeq \frac{4 \times 10^{23}}{A} \frac{\alpha'}{\alpha} \frac{[\text{keV}]}{m_v} \frac{\sigma_{pe}}{[\text{barns}]} \text{kg}^{-1}\text{day}^{-1}. \quad (9)$$

Point-Contact Germanium detectors [10, 4] are ideal devices for the searches of  $\chi_{ps}$  and  $\chi_v$ , due to their low energy threshold which expand the sensitivities to low  $m_\chi$  and excellent energy resolution allows spectral peaks to be resolved. The interaction rates of  $\chi_{ps}$  and  $\chi_v$  with Ge-detector follow Eqs. (8) and (9), respectively, are illustrated in Fig. 1 for specific choices of the coupling constants.

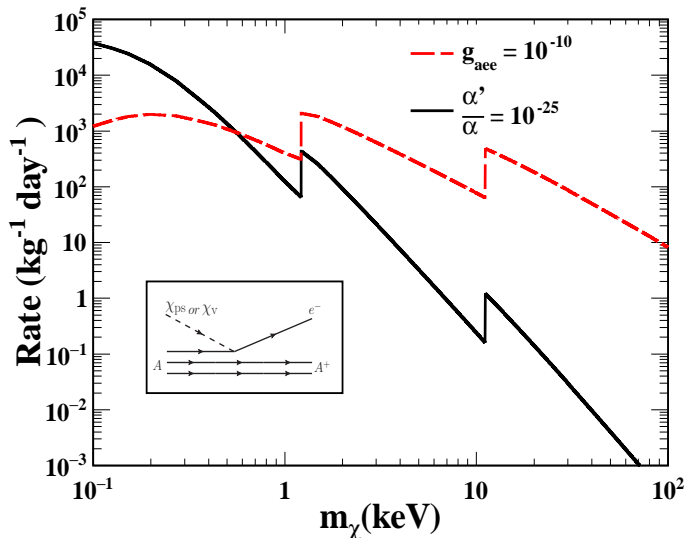


Figure 1: The expected pseudoscalar and vector interaction rates in Ge-detector, for fixed values of  $g_{aee}$  and  $\alpha'/\alpha$ , as a function of  $m_\chi$ . The axioelectric interaction is illustrated schematically in the inset.

The characteristic features in the calculated spectrum at energies 11.10 keV (K-shell) and 1.41 keV (L-shell) correspond to absorption edges of the photoelectric effect in the germanium atom. These features as peaks or edges at the specific binding energies significantly enhance the sensitivity of the experiment compared to the case of a continuum curve.

### 3. Experimental Setup

The TEXONO collaboration [11] aims to progressively improving the sensitivities towards electromagnetic properties of neutrino [12, 13, 14] as well as WIMP [15, 16], axions [17] and physics searches beyond the SM at KSNL. The experimental setup is placed at the first floor of the seven-storey reactor building at depth of  $\sim 12$  m below the sea level. The concrete of the reactor building provides 30 meters of water equivalent overburden, which eliminates most of the hadronic components of cosmic rays. A multipurpose  $4\pi$  passive shielding house with “inner target” detector volume of  $100 \text{ cm} \times 80 \text{ cm} \times 75 \text{ cm}$  con-

sists of, from the inside out, 5 cm of oxygen-free high-conductivity copper, 25 cm of boron-loaded polyethylene, 5 cm of steel, 15 cm of lead. The shielding house is further mounted with cosmic ray (CR) veto scintillator panels. This 50-ton passive shielding house provides significant attenuation to the ambient neutron and  $\gamma$  backgrounds. The Ge-detector surrounded by 38.3 kg well-shaped NaI(Tl) anti-Compton (AC) detector is placed inside the inner target volume. A detailed description of shielding and the detector development at KSNL can be found in Refs. [11, 14, 18].

The data acquisition (DAQ) system in operation at KSNL is a hybrid design of digital and analog electronics. The schematic block-diagram of electronics and DAQ system is illustrated in Fig. 2. The preamplifier of PCGe is custom designed with 5 copies of a signal. Two copies of Ge-preamplifier signal are shaped with Canberra 2026 shaping amplifier (SA) at 6  $\mu s$  and 12  $\mu s$  with same amplification factors. The distinct behavior of self-trigger noise at different shaping time helps to suppress noise events near the threshold. One copy of Ge-preamplifier is processed with SA at minimum gain to study the high energy background behavior. The timing amplifier output (TA) preserves the rise-time information. Therefore, two copies of Ge-preamplifier signal are processed with Canberra 2111 TA at “out” differentiate along with 10  $ns$  integration control setting with different gains to cover a wide energy range from sub-keV to few hundreds keV.

The KSNL readout system is built around National Instruments (NI) PXIe-1065 chassis with an embedded PXI-8108 controller and extended by NI PXI-5105 analog-to-digital converter (ADC), NI PXI-5124 ADC, and NI PXIe-7961R FlexRIO Field Programmable Gate Arrays (FPGA) cards. The NI PXI-5105 ADC with 12-bit resolution, 60 MHz bandwidth and 60 MS/s (MS: Mega sample) real-time sample rate is being used to digitize the signal from shaping amplifiers. The NI PXI-5124 ADC with 12-bit resolution, 200 MS/s real-time sample rate and 150 MHz bandwidth records the signal from timing amplifiers. The NI PXIe-7961R FlexRIO FPGA module composed with high-speed 16-channel, 14-bit and 50 MS/s NI 5751 digitizer-adapter is the heart of the

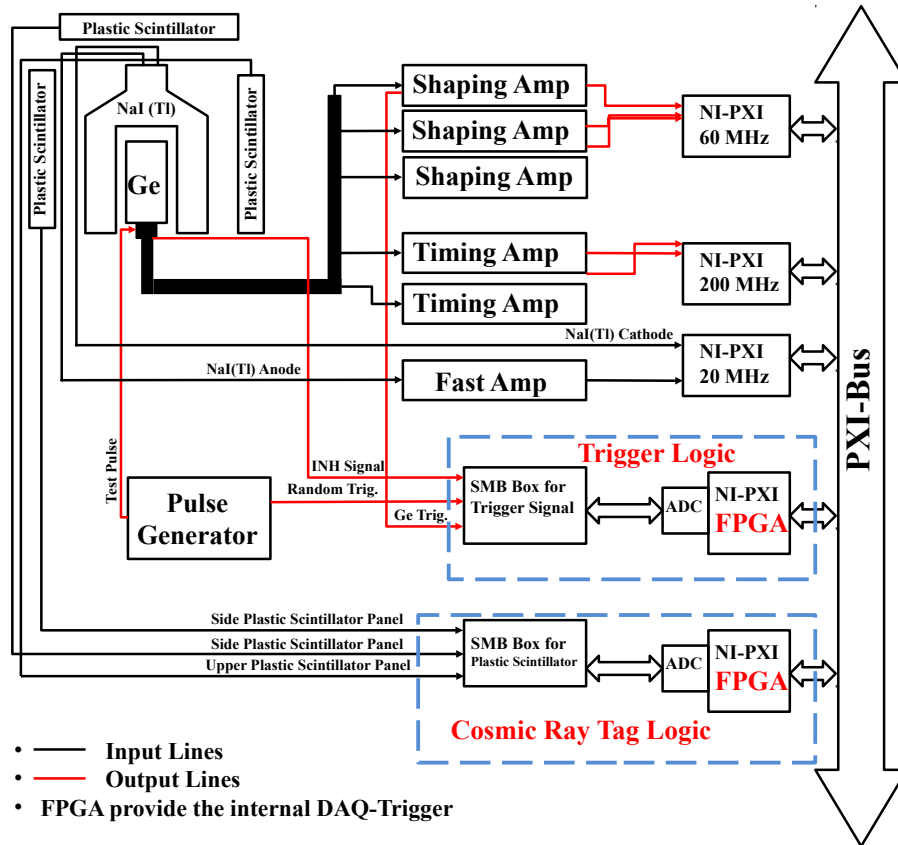


Figure 2: Schematic diagram of the data acquisition system for TEXONO experiment at KSNL.

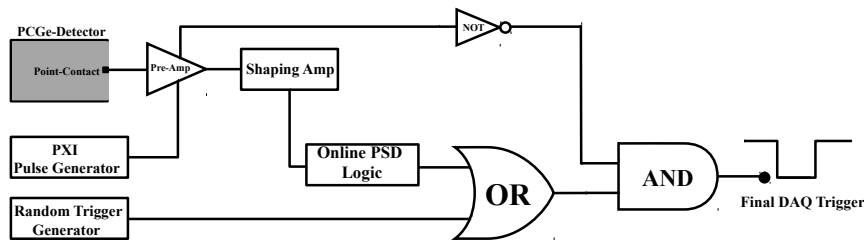


Figure 3: Schematic diagram of data acquisition trigger.



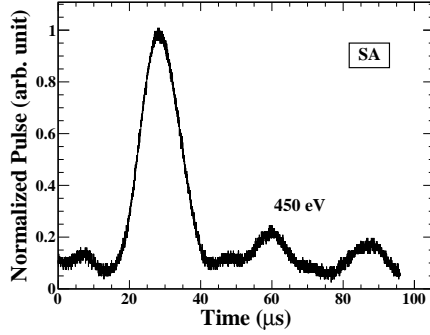


Figure 4: A Typical pulse shape at 450 eV from SA at 6  $\mu s$  output.

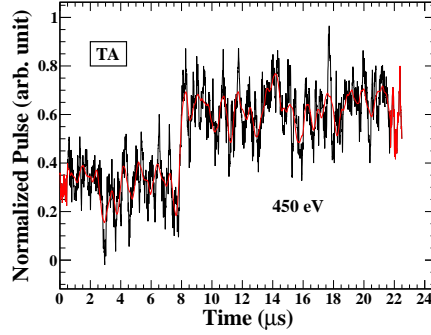


Figure 5: A Typical pulse shape at 450 eV from TA output with raw (black) and smoothed (red) pulse.

DAQ system. These FPGA-modules provide the user-defined logic to specify the trigger condition for CR veto scintillator panels and Ge-detector. It also helps to reject some microphonic noise online, based on distorted pulse shape. The signal from the DC-coupled preamplifier is discriminated after being shaped with SA at 6  $\mu s$  served as a Ge-trigger. The random-trigger is generated by a function generator at the rate of 0.1 Hz and recorded randomly due to OR-gate logic with random Ge-trigger. These random-trigger events help to measure the pedestal fluctuation and dead time of the DAQ system. The inhibit output from the preamplifier is used to veto all triggers generated during the reset of the preamplifier, including random-trigger. A schematic diagram of DAQ trigger scheme at KSNL is shown in Fig. 3. A typical low energy signal from SA and TA is depicted in Fig. 4 and Fig. 5, respectively. The signal of AC NaI-detector and CR veto panel are also recorded along with Ge-trigger to understand the cosmic induced background, and filtered out in the offline analysis. The known amplitude pulses are generated from the precision wave function generator and injected into the test port of the preamplifier to study the trigger efficiency and electronic behavior of the DAQ system. The DAQ software is developed in NI LabVIEW programming language which provides a user-friendly environment. To monitor the data quality, the DAQ software generates cumulative diagnostic

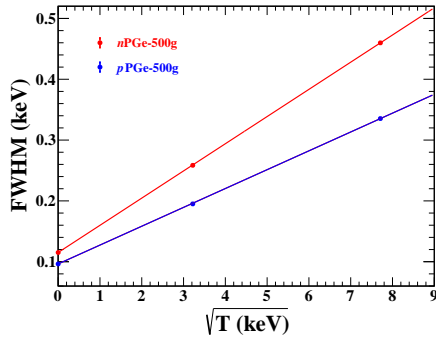


Figure 6: Comparison of energy resolution of  $n$ PCGe and  $p$ PCGe at pedestal fluctuation (0 keV), Ga K-Shell X-ray (10.37 keV) and  $^{241}\text{Am}$   $\gamma$ -ray (59.5 keV).

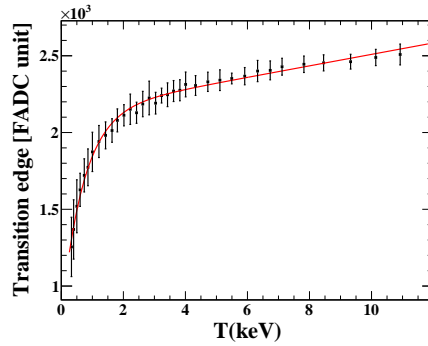


Figure 7: The transition edge of TA-pulses as a function of energy with best fit function.

plots for immediate inspection.

#### 4. Characterization of N-type PCGe-Detector

The energy calibration from sub-keV to 14 keV is achieved by the combination of precise-pulsar measurement and X-ray peaks (10.37 keV and 1.29 keV), resulting from electron capture of Ga daughter induced by cosmogenic  $^{68,71}\text{Ge}$ -isotope. The maximal amplitude and integrated area of the pulse are both energy related parameters. The maximal amplitude is adopted to estimate the energy of an event for its better energy resolution [4, 19]. The energy resolution of  $n$ PCGe is comparable to p-type Point-Contact ( $p$ PCGe) in low energy region, but degraded in high energy region. The energy resolution of  $n$ PCGe may be enhanced by increasing the detector operating temperature, selecting the material with lower electron trap concentrations and higher gradients impurity concentrations to generate higher drift field [20, 10]. Figure 6 illustrates the variation of full width at half maximum (FWHM) as a function of energy for  $n$ PCGe and  $p$ PCGe detectors. The FWHM of  $n$ PCGe degrades as energy deposition increases. The performance parameters of same modular mass  $n$ PCGe and  $p$ PCGe detectors are summarized in Table 1.

Table 1: Comparison between  $n$ PCGe and  $p$ PCGe-detector on basis of various performance parameters. The pulse maximal amplitude is adopted as energy estimator in sub-keV energy region.

Item	$p$ PCGe	$n$ PCGe
Modular Mass (g)	500	500
RESET Amplitude (V)	6.8	6.8
RESET Time Interval (ms)	$\sim 160$	$\sim 170$
Pedestal Noise		
Amplitude RMS $\sigma_{Noise}$ (eV)	41	49
Pulser Width		
FWHM (eV)	110	133
RMS (eV)	47	52
X-Ray Line Width		
RMS (eV)	Ga-K	Ga-K
Electronic Noise-Edge for Raw Spectra (eV )	228	285

Experimental sensitivity for physics beyond the SM is not only limited by signal detection threshold of the Ge-detectors, but also due to the degradation of background rejection capability at sub-keV recoil energy region. The anomalous surface events in  $p$ PCGe arise from a few millimeters thick transition layer with a weak electric field. The poor charge collection in this region reduces the ionization yield of the events and enhances the background at sub-keV energy region. The  $p^+$  outer surface conductive contact of  $n$ PCGe is fabricated with the boron implantation technique. The thickness of  $p^+$  contact on the outer surface of the crystal is the order of  $\mu\text{m}$ . The anomalous surface effect in  $n$ PCGe is studied by the rise time of events. In order to measure the rise time of events, the output of TA is fitted with the hyperbolic tangent function

$$f(t) = \frac{A_0}{2} \tanh[(t - t_0)s_0] + P_0, \quad (10)$$

where  $A_0$ ,  $P_0$ ,  $t_0$  and  $s_0$  are, respectively, the amplitude, pedestal offset, transition edge and slope of the TA-pulse. The values of  $A_0$  and  $P_0$  are evaluated

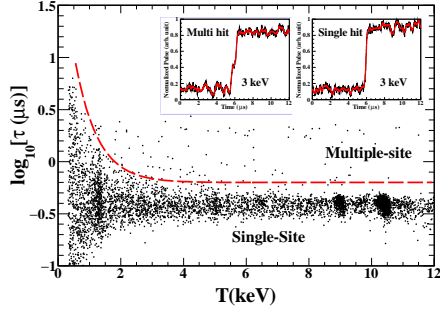


Figure 8: The scatter plot between  $\tau$  and  $T$  for the  $AC^- \otimes CR^-$ -tag events shows absence of anomalous surface events. Typical single- and multiple-site events are shown in inset, multiple-site events are characterized by kinks in rise-time profiles.

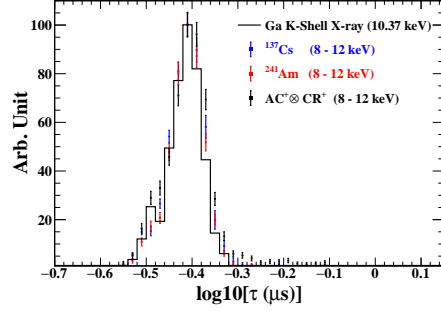


Figure 9: The  $\tau$ -distribution of Ga K-Shell X-ray (10.37 keV), comparing the candidate events with those of  $^{241}\text{Am}$ ,  $^{137}\text{Cs}$  between 8 to 12 keV energy region.

from the TA-pulses through the difference and mid level of asymptotic levels, respectively. The transition edge of TA-pulses as a function of energy is predetermined as shown in Fig. 7 and provides constraint on  $t_0$ . The bending attribute between energy and transition edge of TA-pulse at low energies is due to the difference in shaping times of SA-trigger and TA pulse. The rise time ( $\tau$ ) of TA-pulse is characterized by the slope parameter  $s_0$  and rise time from 5% to 95% is evaluated by  $\tau = \log(19)/s_0$ . The distribution of  $\tau$  as a function of energy is depicted in Fig. 8, which demonstrates the absence of anomalous surface events. The scattered events above the curve (red) in Fig. 8 are identified as multiple sites events. Typical single- and multiple-site events at low energy are illustrated in the inset of Fig. 8. The  $\tau$ -distribution of events from different known origins can verify the uniform timing response over the entire detector fiducial volume. Figure 9 illustrates the uniform timing response for external  $\gamma$ -ray from  $^{241}\text{Am}$ ,  $^{137}\text{Cs}$  and internal X-rays at 10.37 keV from  $^{68,71}\text{Ge}$ , which decay via electron capture.

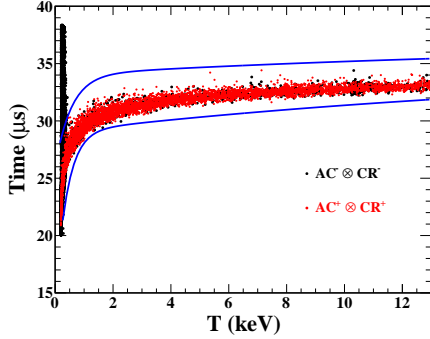


Figure 10: Scatter plot of the correlation between maximum time bin of pulse and corresponding energy.

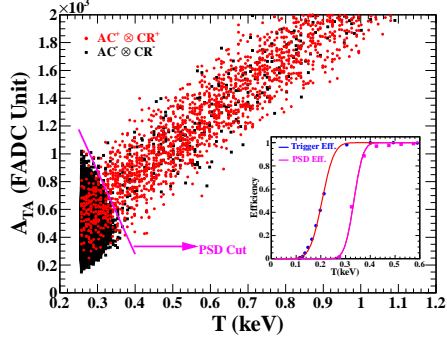


Figure 11: Scatter plot between amplitude of TA-pulse and measured energy  $T$  to illustrate the PSD selection. The inset illustrates the trigger efficiency as a function of energy, along with total PSD efficiency.

## 5. Data Analysis

Data taken with the  $n$ PCGe detector have been adopted to place constraints on milli-charged neutrino [21] and dark matter cosmic ray [22], as well as heavy sterile neutrinos as dark matter [13]. The data presented in this article were acquired over 628.3 live-days (whole exposure) with 500g fiducial mass of  $n$ PCGe-detector. The event information from AC and CR-detectors is recorded along with Ge-trigger. Thus, every Ge-trigger is categorized by  $AC^{+(-)} \otimes CR^{+(-)}$ , where the superscript  $+(-)$  denotes coincidence (anti-coincidence). The  $AC^+ \otimes CR^+$ -tag events are mostly due to energy deposited by radiations in the Ge-detector. These double tagged events serve as the reference samples to differentiate signal from noise.

The  $AC^- \otimes CR^-$ -tag events are uncorrelated with AC and CR active shielding detectors and may be the candidate events of  $\chi$ , neutrino, internal cosmogenically induced background and self-trigger (electronic noise) near the noise-edge. The threshold of Ge-detector is restricted by self-trigger and microphonic noise. In order to avoid the contamination of noise near the detector threshold, it is necessary to define a precise signal acceptance. Therefore, pulse shape dis-

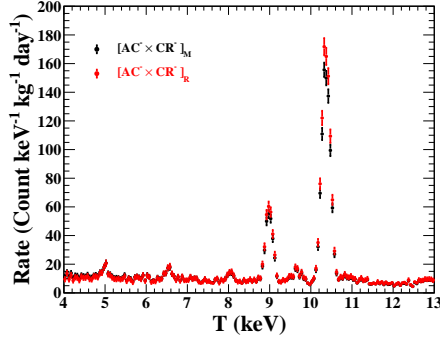


Figure 12: Measured energy spectrum of data sample,  $AC^- \otimes CR^-$  before and after cosmic ray correction.

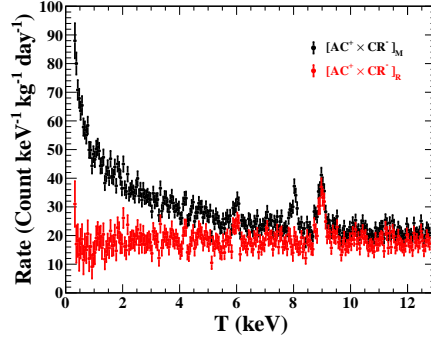


Figure 13: Measured energy spectrum of data sample,  $AC^+ \otimes CR^-$ , before and after cosmic ray correction.

crimination (PSD) technique is adopted to remove a majority of microphonic pulses and define noise edge for analysis. The shaped waveform of Ge-detector is characterized by several parameters. Lowest-level, pedestal (average value of pre-trigger baseline) and maximum time bin are used to discard the most of the noise, which leaks to high energy bins. The maximum time bin of the good pulses lies within a time interval after the trigger. Thus, the amplitude and the maximum time bin of the signal pulse exhibit the strong correlation as shown in Fig. 10, and all events outside the correlated band are rejected. In order to define the noise edge between self-trigger and physics events, the energy of event and amplitude of TA-pulse ( $A_{TA}$ ) after process with the trapezium-filter provide one of the best possible parameter space. Figure 11 shows the distribution of  $AC^- \otimes CR^-$  and  $AC^+ \otimes CR^+$  with the noise-edge cut. The fraction of  $AC^+ \otimes CR^+$ -tag events survives as an efficiency of the PSD cuts. The trigger efficiency measured by survival fraction of precise pulser at given trigger threshold. The trigger efficiency and combined PSD efficiency is 100% above 300 eV and 400 eV, respectively, as shown in the inset of Fig. 11.

Cosmic ray muon detection efficiency of CRV system on average for a week period is typically 93%, and the rejection efficiency of cosmic ray induced event by timing correlation between Ge-trigger and CR-trigger is 92%. The measured

$AC^- \otimes CR^-$  spectrum therefore could be contaminated with cosmic ray induced events. The presence of additional cosmic events in the residual energy spectrum of  $AC^- \otimes CR^-$  events is suppressed by the statistical background model. The real cosmic ( $T_r$ ) and non-cosmic ( $V_r$ ) event rate can be correlated with measured ( $V_m, T_m$ ) rate via following couple of equations

$$V_r = \frac{\lambda_{crv}}{\epsilon_{crv} + \lambda_{crv} - 1} \cdot V_m - \frac{1 - \lambda_{crv}}{\epsilon_{crv} + \lambda_{crv} - 1} \cdot T_m \quad \text{and} \quad (11)$$

$$T_r = \frac{\epsilon_{crv}}{\epsilon_{crv} + \lambda_{crv} - 1} \cdot T_m - \frac{1 - \epsilon_{crv}}{\epsilon_{crv} + \lambda_{crv} - 1} \cdot V_m, \quad (12)$$

where  $\epsilon_{crv}$  is the rejection efficiency of cosmic ray cut and  $\lambda_{crv}$  is the detection efficiency of cosmic ray system. The verification of the correction method is provided by the intensity of known K-shell internal X-rays and ambient  $\gamma$ -ray energy spectrum. The intensities of K-shell X-rays increased by putting back leakage events into their own sample, as illustrated in Fig. 12. High energy  $\gamma$ -rays from ambient radioactivity produce flat electron-recoil background at low energy, which is verified by simulation and measurements ( $^{241}\text{Am}$  and  $^{137}\text{Cs}$  source). Figure 13 demonstrates the flat energy spectra after correction for  $AC^+ \otimes CR^-$  data sample.

The observed  $AC^- \otimes CR^-$  spectra with internal X-ray lines from cosmogenically-induced isotopes decays via electron capture process is shown in Fig. 14.

The intensity of K-shell peaks decay with time and low energy L-capture lines corresponding to  $^{65}\text{Zn}$  and  $^{68}\text{Ge}$  behaves similar to high energy K-capture lines. The L/K-capture ratio from the same isotope has been well understood by theoretically and independent experimental measurements. Therefore, the intensities of L-shell X-ray lines are estimated from measured K-shell X-ray lines and subtracted from measured  $AC^- \otimes CR^-$  spectra. The predicted intensities of L-shell X-ray lines are depicted in the inset of Fig. 14.

## 6. Experimental Constraints

The signal of nonrelativistic  $\chi$  would be  $\delta$ -function centered at its mass, smearing by the energy resolution of the detector. The expected signal rate of

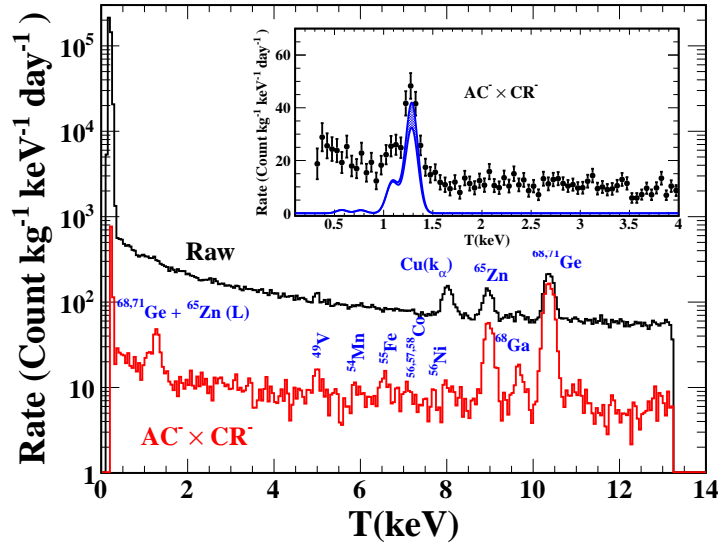


Figure 14: Measured Raw and  $AC^- \otimes CR^-$  spectra with  $nPCGe$ , the L-shell X-ray lines predicted from the intensities of measured K-shell X-ray lines is shown in inset.

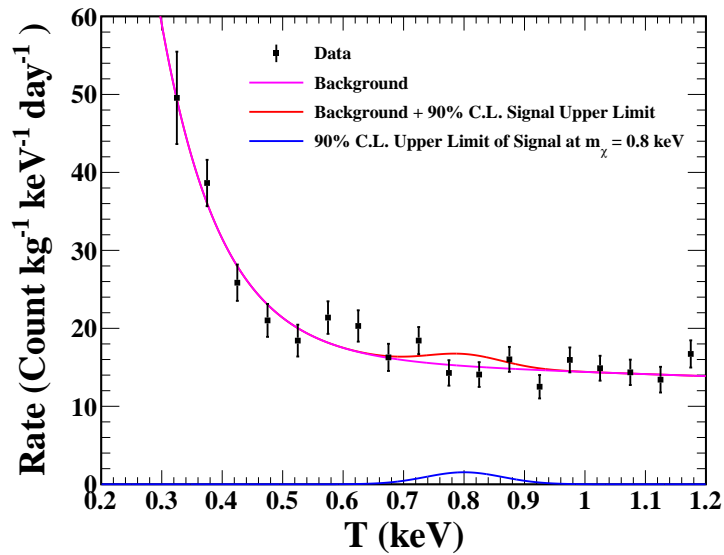


Figure 15: The efficiency-corrected energy spectrum near to the analysis threshold with the whole exposure. An example of excluded rate (90% C.L.) at 0.8 keV for non-relativistic bosonic  $\chi$  signal is shown with blue curve. The assumption of flat plus exponential background is also superimposed.



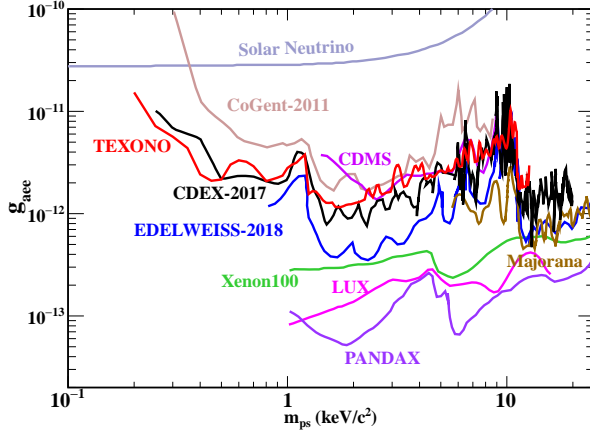


Figure 16: Constraints on  $g_{aee}$  of  $\chi_{ps}$  as a function of mass. The TEXONO upper limits, at 90% C.L. is shown in red curve. Results from representative experiments CDEX [23], CoGeNT [24], EDELWEISS [25], LUX [26], Majorana Demonstrator [27], PANDAX-II [28], XENON100 [29] along with indirect astrophysical bound from solar neutrinos [30] are also shown.

$\chi$  at measurable energy is obtained by the convolution of interaction rate from Eq. (8) or (9) with the energy resolution of the detector:

$$\frac{dR_\chi}{dE}(E, m_\chi) = \Phi_\chi(m_\chi)\sigma_\chi \times \frac{1}{\sqrt{2\pi}\sigma_E(m_\chi)} e^{-\frac{(E-m_\chi)^2}{2\sigma_E^2(m_\chi)}} \quad (13)$$

where  $\chi = \chi_{ps}$ ,  $\chi_v$  represents pseudoscalar and vector particles, respectively. A minimal-chi-square analysis is applied with free parameters describing a flat plus exponential background and coupling constant of  $\chi$ . Our data are compatible with the background only hypothesis, and no excess of events are observed over the background as depicted in Fig. 15. The 90% confidence level (C.L.) excluded rate in  $\text{kg}^{-1}\text{day}^{-1}$  for a given  $m_\chi$  is evaluated from best fit parameters. The excluded value of coupling constant is then derived from excluded count rate using Eqs. (8) or (9). The 90% C.L. exclusion limits for coupling of  $\chi_{ps}$  as a function of  $m_\chi$  are shown in Fig. 16, results from other representative experiments are also superimposed.

The upper limits on the electronic coupling of  $\chi_v$  at 90% C.L. are derived using the same data and analysis technique. Figure 17 shows the exclusion

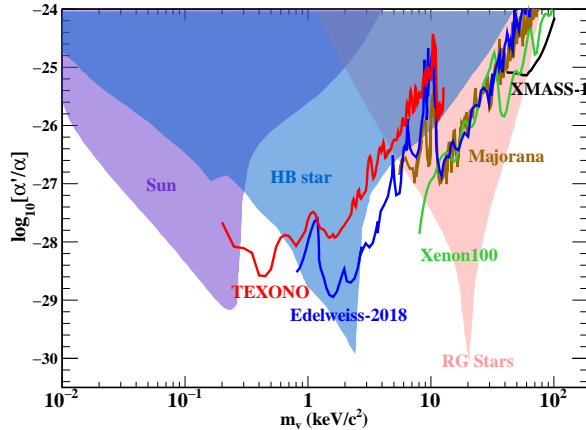


Figure 17: The 90% C.L. bounds on vector bosonic DM coupling from the TEXONO compared with astrophysical sources [9] as well as experimental results from EDELWEISS [25], Majorana Demonstrator [27], XENON100 [31] and XMASS-I [32].

limits at 90% C.L. of electronic coupling of  $\chi_v$ . The laboratory upper limits on vector-electric coupling established by direct detection experiments are potentially more stringent than limits derived from cosmological and astronomical sources. The observed fluctuations in the exclusion curve correspond to statistical fluctuations in the background. Our data with sub-keV sensitivity provide the improved constraints on electronic couplings of pseudoscalar and vector bosonic DM in sub-keV/ $c^2$  mass region.

## 7. Conclusion and prospects

New constraints on dark matter candidates  $\chi_{ps}$  and  $\chi_v$  with  $n$ PCGe are presented in this article. This detector technique provides low threshold, excellent energy resolution and without complications of anomalous surface background events. It is therefore an optimal detector to study not just  $\chi$  but also milli-charged neutrino [21] and dark matter WIMPs [33], as well as dark matter heavy sterile neutrinos [13]. Data taking continues at KSNL with improved PCGe detectors. The goals are to enhance the sensitivities of these measurements, as well as to study the standard model neutrino-nucleus coherent scattering [4, 34, 11].

## 8. Acknowledgments

This work is supported by the 2017-21 Academia Sinica Investigator Award AS-IA-106-M02, as well as contracts MOST 107-2119-M-001-028-MY3 from the Ministry of Science and Technology, and 2017-18/ECP-2 from the National Center of Theoretical Physics, Taiwan.

## References

- [1] E. Aprile, et al., Dark matter search results from a one ton-year exposure of xenon1t, *Phys. Rev. Lett.* 121 (2018) 111302. doi:10.1103/PhysRevLett.121.111302.
- [2] X. Cui, et al., Dark Matter Results From 54-Ton-Day Exposure of PandaX-II Experiment, *Phys. Rev. Lett.* 119 (18) (2017) 181302. doi:10.1103/PhysRevLett.119.181302.
- [3] M. Pospelov, A. Ritz, M. Voloshin, Bosonic super-wimps as keV-scale dark matter, *Phys. Rev. D* 78 (2008) 115012. doi:10.1103/PhysRevD.78.115012.
- [4] A. K. Soma, et al., Characterization and Performance of Germanium Detectors with sub-keV Sensitivities for Neutrino and Dark Matter Experiments, *Nucl. Instrum. Meth. A* 836 (2016) 67–82. doi:10.1016/j.nima.2016.08.044.
- [5] P. Arias, et al., Wispy cold dark matter, *Journal of Cosmology and Astroparticle Physics* 2012 (06) 013. doi:10.1088/1475-7516/2012/06/013.
- [6] A. E. Nelson, J. Scholtz, Dark light, dark matter, and the misalignment mechanism, *Phys. Rev. D* 84 (2011) 103501. doi:10.1103/PhysRevD.84.103501.
- [7] A. Arvanitaki, J. Huang, K. Van Tilburg, Searching for dilaton dark matter with atomic clocks, *Phys. Rev. D* 91 (2015) 015015. doi:10.1103/PhysRevD.91.015015.

- [8] S. Dimopoulos, G. D. Starkman, B. W. Lynn, Atomic enhancements in the detection of weakly interacting particles, *Physics Letters B* 168 (1) (1986) 145 – 150. doi:10.1016/0370-2693(86)91477-2.
- [9] H. An, M. Pospelov, J. Pradler, A. Ritz, Direct detection constraints on dark photon dark matter, *Physics Letters B* 747 (2015) 331 – 338. doi:10.1016/j.physletb.2015.06.018.
- [10] P. S. Barbeau, J. I. Collar, O. Tench, Large-Mass Ultra-Low Noise Germanium Detectors: Performance and Applications in Neutrino and Astroparticle Physics, *JCAP* 0709 (2007) 009. doi:10.1088/1475-7516/2007/09/009.
- [11] H. T. Wong, Taiwan experiment on neutrino history and prospects, *International Journal of Modern Physics A* 33 (16) (2018) 1830014. doi:10.1142/S0217751X18300144.
- [12] J.-W. Chen, et al., Constraining neutrino electromagnetic properties by germanium detectors, *Phys. Rev. D* 91 (2015) 013005. doi:10.1103/PhysRevD.91.013005.
- [13] J.-W. Chen, et al., Atomic ionization by sterile-to-active neutrino conversion and constraints on dark matter sterile neutrinos with germanium detectors, *Phys. Rev. D* 93 (2016) 093012. doi:10.1103/PhysRevD.93.093012.
- [14] H. T. Wong, et al., Search of neutrino magnetic moments with a high-purity germanium detector at the kuo-sheng nuclear power station, *Phys. Rev. D* 75 (2007) 012001. doi:10.1103/PhysRevD.75.012001.
- [15] H. B. Li, et al., Limits on spin-independent couplings of wimp dark matter with a *p*-type point-contact germanium detector, *Phys. Rev. Lett.* 110 (2013) 261301. doi:10.1103/PhysRevLett.110.261301.
- [16] S. T. Lin, et al., New limits on spin-independent and spin-dependent couplings of low-mass wimp dark matter with a germanium detector at

- a threshold of 220 eV, Phys. Rev. D 79 (2009) 061101. doi:10.1103/PhysRevD.79.061101.
- [17] H. M. Chang, et al., Search for axions from the kuo-sheng nuclear power reactor with a high-purity germanium detector, Phys. Rev. D 75 (2007) 052004. doi:10.1103/PhysRevD.75.052004.
- [18] M. Deniz, et al., Measurement of  $\bar{\nu}_e$ -electron scattering cross section with a csi(tl) scintillating crystal array at the kuo-sheng nuclear power reactor, Phys. Rev. D 81 (2010) 072001. doi:10.1103/PhysRevD.81.072001.
- [19] M. K. Singh, et al., Characterization of the sub-keV germanium detector, Indian Journal of Physics 92 (3) (2018) 401–408. doi:10.1007/s12648-017-1116-x.
- [20] P. N. Luke, et al., Low capacitance large volume shaped-field germanium detector, IEEE Transactions on Nuclear Science 36 (1) (1989) 926–930. doi:10.1109/23.34577.
- [21] J.-W. Chen, et al., Constraints on millicharged neutrinos via analysis of data from atomic ionizations with germanium detectors at sub-keV sensitivities, Phys. Rev. D 90 (2014) 011301. doi:10.1103/PhysRevD.90.011301.
- [22] L. Singh, et al., Constraints on millicharged particles with low threshold germanium detectors at Kuo-Sheng Reactor Neutrino Laboratory arXiv:1808.02719.
- [23] S. K. Liu, et al., Constraints on axion couplings from the cdex-1 experiment at the china jinping underground laboratory, Phys. Rev. D 95 (2017) 052006. doi:10.1103/PhysRevD.95.052006.
- [24] C. E. Aalseth, et al., Results from a search for light-mass dark matter with a  $p$ -type point contact germanium detector, Phys. Rev. Lett. 106 (2011) 131301. doi:10.1103/PhysRevLett.106.131301.

- [25] E. Armengaud, et al., Searches for electron interactions induced by new physics in the EDELWEISS-III Germanium bolometers [arXiv:1808.02340](#).
- [26] D. S. Akerib, et al., First searches for axions and axionlike particles with the lux experiment, *Phys. Rev. Lett.* 118 (2017) 261301. doi:10.1103/PhysRevLett.118.261301.
- [27] N. Abgrall, et al., New limits on bosonic dark matter, solar axions, pauli exclusion principle violation, and electron decay from the majorana demonstrator, *Phys. Rev. Lett.* 118 (2017) 161801. doi:10.1103/PhysRevLett.118.161801.
- [28] C. Fu, et al., Limits on axion couplings from the first 80 days of data of the pandax-ii experiment, *Phys. Rev. Lett.* 119 (2017) 181806. doi:10.1103/PhysRevLett.119.181806.
- [29] E. Aprile, et al., Erratum: First axion results from the xenon100 experiment [*phys. rev. d* 90, 062009 (2014)], *Phys. Rev. D* 95 (2017) 029904. doi:10.1103/PhysRevD.95.029904.
- [30] P. Gondolo, G. G. Raffelt, Solar neutrino limit on axions and keV-mass bosons, *Phys. Rev. D* 79 (2009) 107301. doi:10.1103/PhysRevD.79.107301.
- [31] E. Aprile, et al., Search for bosonic super-wimp interactions with the xenon100 experiment, *Phys. Rev. D* 96 (2017) 122002. doi:10.1103/PhysRevD.96.122002.
- [32] K. Abe, et al., Search for bosonic superweakly interacting massive dark matter particles with the xmass-i detector, *Phys. Rev. Lett.* 113 (2014) 121301. doi:10.1103/PhysRevLett.113.121301.
- [33] H. Jiang, et al., Limits on light weakly interacting massive particles from the first 102.8 kg  $\times$  day data of the cdex-10 experiment, *Phys. Rev. Lett.* 120 (2018) 241301. doi:10.1103/PhysRevLett.120.241301.

- [34] S. Kerman, V. Sharma, M. Deniz, H. T. Wong, J.-W. Chen, H. B. Li, S. T. Lin, C.-P. Liu, Q. Yue, Coherency in neutrino-nucleus elastic scattering, *Phys. Rev. D* 93 (2016) 113006. doi:10.1103/PhysRevD.93.113006.